5-2016

Magnetism of Magnetite nanoparticles as determined by Mössbauer Spectroscopy

Hien-Yoong Hah
University of Tennessee - Knoxville, hhah@utsi.edu

To the Graduate Council:

I am submitting herewith a thesis written by Hien-Yoong Hah entitled "Magnetism of Magnetite nanoparticles as determined by Mössbauer Spectroscopy." I have examined the final electronic copy of this thesis for form and content and recommend that it be accepted in partial fulfillment of the requirements for the degree of Master of Science, with a major in Biomedical Engineering.

Jacqueline A. Johnson, Major Professor

We have read this thesis and recommend its acceptance:

Silke Hecht, Claudia Rawn

Accepted for the Council:
Carolyn R. Hodges

Vice Provost and Dean of the Graduate School

(Original signatures are on file with official student records.)

Magnetism of Magnetite nanoparticles as determined by Mössbauer Spectroscopy

A Thesis Presented for the
Master of Science
Degree
The University of Tennessee, Knoxville

Hien-Yoong Hah
May 2016

Acknowledgements

I would like to thank my parents, my mum in particular for being greatly supportive of my education. My siblings for keeping me in line. Dr Jackie and Dr Charles Johnson for advice and help on the writing. Sharon Gray and Jared Alberts for being the best of friends. Adam Evans, Lee Leonard and Julie Swafford for being kindred spirits. Dr Silke Hecht and Dr Claudia Rawn for agreeing to be on my committee.

Abstract

Fe_3O_4 [Magnetite] nanoparticles have magnetism that differs greatly from their bulk counterparts. Whereas bulk Fe_3O_4 is a ferrimagnet, single-domain Fe_3O_4 nanoparticles have been found to be superparamagnetic. This allows for increased magnetization of the nanoparticles compared to the bulk when in a magnetic field. For most paramagnets, magnetization requires applied fields of a few Tesla at low temperatures. This is achievable through the application of superconducting magnets. In superparamagnets, the high susceptibility of the particles allows magnetization through a Nd-Fe-B permanent magnet at room temperature. This is caused by an increased number of magnetic atoms within the particles, which greatly increases susceptibility of the particles. ^{57}Co [Cobalt-57] Mössbauer Spectroscopy allows the probing of the internal environment of an iron nucleus, which gives insight into the magnetic properties of the Fe_3O_4 nanoparticles.

Table of Contents

List of Tables

List of Figures

CHAPTER I INTRODUCTION

This thesis is a Mössbauer study of superparamagnetic iron oxide nanoparticles (SPIONs), which can be synthesized in large quantities with a narrow size distribution. SPIONs have numerous applications in biomedical science and engineering such as hyperthermia, drug delivery systems, magnetic resonance imaging, cell separation, and biosensing, to name a few.

Iron Oxide Nanoparticles

Magnetic properties of iron oxides vary greatly depending on the phase and stoichiometry of the materials. In this work, magnetite (Fe_3O_4) nanoparticles are discussed. Recently, magnetic properties in iron oxide nanoparticles have been found to be useful in medical imaging, most notably as contrast agents for Magnetic Resonance Imaging (MRI) [1]. Current contrast agents, such as gadolinium, are based on the modification of T1 relaxation time (spin-lattice) in water molecules, while iron oxide nanoparticles modify T2 relaxation time (spin-spin) of nearby protons in water molecules. Furthermore, due to the ability of magnetic nanoparticles to generate heat through excitation at certain radio frequencies, these nanoparticles can be used to destroy targeted cells in the body. Cancerous cells in the body need an increase in temperature to 42 $^{\circ}$C to achieve this effect [2]. Since the best control of these nanoparticles can be achieved through the highest magnetization per volume, nano-sized particles are generally preferable, to decrease demagnetization effects in bulk materials. At these sizes, the nanoparticles are superparamagnets (paramagnets with high magnetic susceptibility), allowing them to be magnetized with a small, applied magnetic field.

Fe_3O_4 has an inverse spinel structure at room temperature [3], which is a cubic crystal system. While all spinel-type materials have the arrangement $X^{2+}Z^{3+}{}_2O^{2-}{}_4$, an inverse spinel has half of

the Z species occupying the tetrahedral sites while the other half shares octahedral sites with the X species. Fe_3O_4, can be written as $(Fe^{3+})_A(Fe^{3+}Fe^{2+})_BO^{2-}{}_4$ [4], where by convention, the A sites are tetrahedral and the B sites are octahedral. Iron atoms at the A sites will be surrounded by 4 oxygen atoms, while Fe^{2+} and Fe^{3+} atoms at the B sites will be surrounded by 6 oxygen atoms [5] [6].

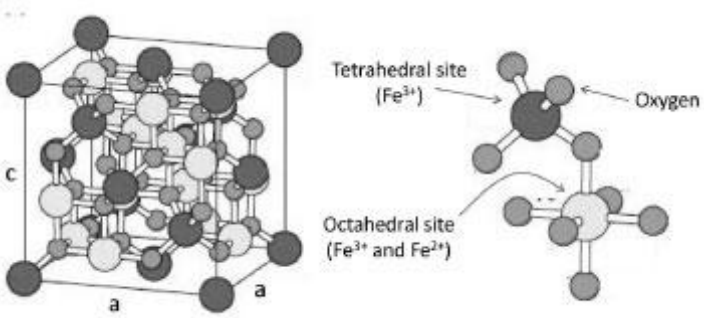

Figure 1: Magnetite crystal structure.

Verwey Transition

In bulk magnetite (Fe_3O_4), a transition exists (between 119 K–122 K) where the resistivity of iron oxide increases with decreasing temperature [7]. Verwey himself believed that this is caused by a decline in "electron hopping" [8] when approaching lower temperatures. As mentioned earlier, Fe_3O_4 has both Fe^{2+} and Fe^{3+} at the same crystallographic site; Verwey suggests that at the B-site, there is electron hopping between two Fe^{3+} ions. Thermal energy from the ambient environment at higher temperatures provides energy to overcome a "hopping" barrier. At lower temperatures, since there is less thermal energy, the barrier becomes prohibitive to electron hopping, which increases the resistivity of magnetite. Due to this hopping, some prefer to

describe the structural formula of Fe_3O_4 as $(Fe^{3+})_A(2Fe^{2.5})_BO^{2-}{}_4$ instead of $(Fe^{3+})_A(Fe^{3+}Fe^{2+})_BO^{2-}{}_4$ that was discussed earlier [9].

Magnetism of Magnetite

Electrons (and nuclei) have an intrinsic spin, which creates a magnetic moment. These magnetic moments align along the easy axes, where the lowest energy state is possible.

Here, three types of magnetism, including ferromagnetism, ferrimagnetism and paramagnetism will be discussed. Paramagnets [10] have magnetic moments that are randomly oriented when no external field is applied. For Mössbauer Spectroscopy, a paramagnet would have a single line spectrum. Ferromagnetism and ferrimagnetism, which commonly exist in permanent magnets, are generally used to describe materials that have net positive magnetic moments. In ferromagnetism, the magnetic moments are all in one direction (Figure 2) while in ferrimagnetism, there are opposing magnetic moments as well. However, since these opposing magnetic moments are smaller in magnitude, there still exists a net positive magnetic moment. In Fe_3O_4, both Fe^{2+} and Fe^{3+} in the octahedral site B have magnetic moments pointing in opposite direction of Fe^{3+} in the tetrahedral site A (Figure 3). The net positive moment is contributed by the Fe^{2+} since the opposite Fe^{3+} in the A and B sites cancel. As a result, Mössbauer Spectroscopy for Fe_3O_4 will have two sextets, one for the tetrahedral A site, and another for the octahedral B site.

At the atomic level, the difference between a paramagnet and a ferro/ferrimagnet is the tendency of the magnetic moments in a ferro/ferrimagnetic material to align in the same direction, due to that particular direction being its lowest energy state (resulting in a net magnetic moment), whereas paramagnets have lower energy in their non-aligned states.

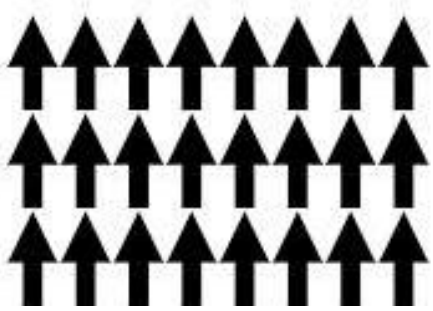

Figure 2: Magnetic moments inside a ferromagnetic material.

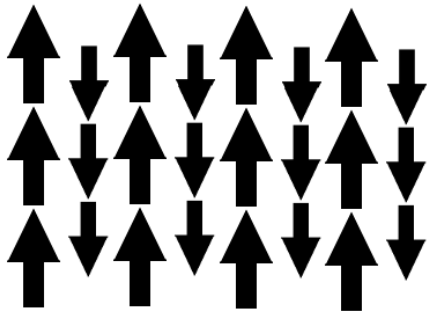

Figure 3: Magnetic moments inside a ferrimagnetic material.

Magnetic Anisotropy

Magnetic anisotropy (*K*) is the energy per unit volume required to bind the magnetic moments along the easy axis [11]. In bulk materials, the magnetic anisotropy is different due to the bulk and nanoparticles having differing number of domains [12]. These domains tend to be oriented in a disordered, non-aligned manner along their own easy axes.

Curie Temperature

Above the Curie temperature of a material, a ferro/ferrimagnetic material will cease to be ferro/ferrimagnetic and become a paramagnet. This also means that without an applied magnetic

field, the magnetic moments in the material above the Curie temperature will be non-aligned, resulting in the net zero external magnetic field. The thermal energies from the higher temperature environment above the Curie temperature allow the magnetic moments to acquire enough energy to overcome the regular alignment of magnetic moments for ferro/ferrimagnetic materials. The Curie temperature of Fe_3O_4 is 858 K.

Superparamagnetism

A superparamagnetic material is a material that has paramagnetic behavior when below its bulk material Curie temperature. Superparamagnetism exists in very small ferro/ferrimagnetic particles, which have magnetic moments that flip continuously, with the moments flipping between directions 180° to each other [14]. The mean time between flips is called the Néel relaxation time [15]. These two antiparallel directions are the stable orientations for the magnetic moments and also define the easy axis for the magnetic moments. Néel relaxation happens due to having a small energy barrier compared to kT (Equation 2), which results in a lower energy barrier [13]. This energy barrier can be given by:

$$E = KV \quad (1)$$

where V is the volume of the particle. Quite simply, it can be seen from Equation 1 that the smaller the particle, the smaller the energy needed to overcome the energy barrier.

Consequently, certain superparamagnetic particles can flip just through the influence of ambient room temperature.

Following Néel's theory of superparamagnetism [16], the relaxation time τ_N of particles with volume V, magnetic anisotropy *K*, *k* the Boltzmann's constant and *T* the temperature, have the Néel relation:

$$\tau_N = \tau_0 \, exp\left(\frac{KV}{kT}\right) \quad (2)$$

τ_0 is the characteristic relaxation time, which is particular to each material, and is 10^{-11}–10^{-9} seconds. It is easy to see from this equation that for a particle with very small volume, the relaxation time τ_N decreases.

Blocking Temperature

Temperature is a factor in the relaxation time—decreasing the temperature increases the relaxation time of the magnetic moments. For Mössbauer Spectroscopy, which is the main probe for the work here, a material with relaxing magnetic moments can be observed. The blocking temperature [17] is the temperature where Mössbauer Spectroscopy is able to resolve the lines in the spectrum. If τ_m is the measurement time for Mössbauer Spectroscopy, then when $\tau_m >> \tau_N$, the hyperfine spectra will not be resolved and considered "unblocked. The blocking temperature is not reached and the spectrum will not be Zeeman-split. However if the opposite situation where $\tau_m << \tau_N$, were to occur, then a "blocked" spectrum with sharp resolved lines will be achieved. The relation for the blocking temperature is:

$$T_B = aKV/k \quad (3)$$

where $a = 1/ln(\tau_m/\tau_0)$.

The Mössbauer Effect

Rudolf Mössbauer discovered the effect named for him in 1957 and was awarded the Nobel Prize in 1961. The Mössbauer Effect is the recoil-free emission and resonant absorption of nuclear gamma rays in solids. Before the discovery of the Mössbauer Effect it was thought that atoms could be considered free as far as nuclear reactions were concerned, because the energy of

nuclear events is so much larger than those associated with chemical binding. The Mössbauer Effect is based on the fact that this is not necessarily so. Mössbauer Spectroscopy is now a standard, very high-resolution technique used to investigate nucleic environments. One isotope that exhibits this effect is ^{57}Fe, which is the isotope used for the experiments presented in this thesis. A brief overview on the Mössbauer Effect [18] will be given here.

A gamma ray photon may be emitted from a free nucleus, which is in an excited state with energy E_0 above the ground state. When this happens the nucleus suffers recoil and the gamma ray is emitted with energy

$$E_\gamma = E_0 - E_R$$

where

$$E_R = {E_0}^2/2Mc^2$$

M is the mass of the recoiling nucleus and c is the velocity of light. For the absorption process, when dealing with an identical nucleus, an energy:

$$E_\gamma = E_0 + E_R$$

is required.

The uncertainty in energy (linewidth) for the nuclear excited state is

$$\Gamma = \hbar/\tau$$

where τ is the mean lifetime of the nuclear state. Therefore if $2E_R >> \Gamma$, resonant absorption of the emitted gamma ray cannot take place for a free atom, see Figure 4.

When the nuclei are embedded in a rigid lattice, however, the whole solid may take up the recoil momentum. The recoil energy, E_R, is proportional to $1/M_S$, where M_S is the mass of the solid and much larger than the mass M of a single nucleus. The recoil energy is then negligible and the

emitted photons have energy close to E_0. Emitted photons can therefore be resonantly absorbed by identical nuclei. In real solids the nuclei are bound in the lattice but are free to vibrate about their mean positions, which leads to thermal broadening. The emission and absorption of gamma rays can be accompanied by the excitation of quantized phonons. For low recoil energies there is a finite probability, f, that no phonons will be excited. In this case $E_R = 0$ and there is no thermal broadening.

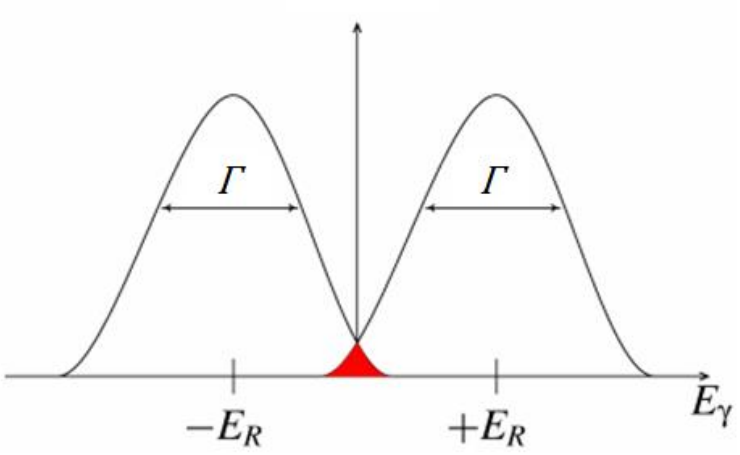

Figure 4: The difference in energy between an emitted and absorbed gamma ray for a free nucleus.

The portion of the decay that does not involve phonons is called the recoil-free fraction. This is the essence of the Mössbauer Effect. The probability, f, for the low temperature approximation is given by:

$$f = exp\left(-\frac{E_R}{k{\theta_d}^2}\left(\frac{3}{2}+\frac{\pi^2T^2}{{\theta_d}^2}\right)\right) \quad (4)$$

It is immediately obvious from the equation that the lower the temperature, the higher the probablility, f [19].

There have been more than 25 isotopes used in Mössbauer spectroscopy, but the isotope ^{57}Fe has the advantageous combination of low gamma-ray energy and long lifetime in its first excited state for the work here. The 14.4 keV gamma-ray transition is used to perform all experiments in this thesis. Its decay scheme is shown in Figure 5.

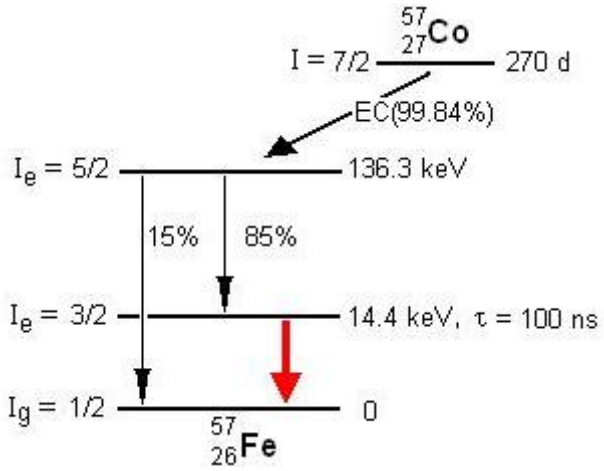

Figure 5: Decay scheme of ^{57}Co yielding ^{57}Fe.

CHAPTER II EXPERIMENTAL RESULTS

Synthesis of iron oxide nanoparticles

Reagents and solvents from commercial sources were: anhydrous iron (II) chloride (99.5%) and iron (III) chloride (98%) from Alfa Aesar; diethylene glycol (DEG) (99%) and 1,2,4benezenetricarboxylic and 5-hydroxyisophthalic acids from Aldrich; sodium metal from Fisher Scientific; and anhydrous citric, malic and L(+)-tartaric acids from ACROS Organics. Prior to use, the solvent diethylene glycol was degassed in a vacuum under stirring for at least 1 h. Synthesis and manipulations with air-sensitive materials were performed in an ultrapure nitrogen atmosphere in a Vacuum Atmospheres Company (VAC) glovebox using the Schlenk technique [20]. These samples were prepared as colloids by our collaborators at Xavier University, the details of which appear in Goloverda *et al* [20]. In order to isolate the product in a powder form for Mössbauer measurements, aliquots of the colloid were precipitated with 1.5 times volumes of ethyl acetate compared to the colloid (assisted by centrifugation and magnetic separation). The solid was then decanted, washed with methanol 2–3 times and dried at room temperature under a flow of nitrogen. Using vacuum grease, which is transparent to the gamma rays, as an adhesive, the samples were placed in the bottom of a custom-made sample holder shown on the left in Figure 6. The top cap, shown on the right in Figure 6, was then inserted to secure the sample.

Figure 6: Mössbauer sample holder, bottom (left) and top (right).

Mössbauer setup

The Mössbauer setup consists of a vibrating source (to vary the energy range), an absorber/sample and a detector (Figure 7). The intensity of gamma rays transmitted through an absorber is measured as a function of the gamma ray energy, which is varied by moving the source relative to the absorber. This results in a Doppler shift of the gamma-ray energy:

$E(v) = E_\gamma + (1+ v/c)$,

where v is the velocity of the source and c is the velocity of light.

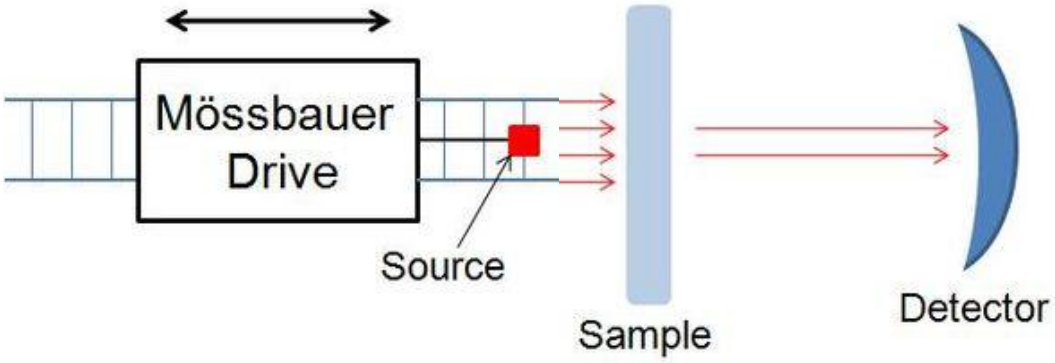

Figure 7: Mössbauer experimental setup.

The Mössbauer resonant absorption occurs only for velocities where the Doppler shifted gamma-ray energy matches a transition in the absorbing nucleus. The velocity of this movement (usually measured in $mm \cdot s^{-1}$) then becomes the Mössbauer energy scale. A velocity of 1 $mm \cdot s^{-1}$ corresponds to 4.804 x 10^{-7} eV for the 14.4 keV gamma rays of ^{57}Fe. The experimental linewidth, 10^{-8} eV, is usually smaller than any of the hyperfine interactions of nuclei with their surrounding electrons. The intra-nuclear forces are larger than the hyperfine interactions by a factor of about 10^{10}. This interaction gives rise to quantized energy levels within the nucleus,

which have a nuclear spin quantum number, I. Neglecting the other interactions, there are (2I + 1) degenerate levels for each value of I. The hyperfine interactions arise from the interactions of the nucleus with electrons of the same atom and those of neighboring atoms. The electric monopole interaction causes a shift in the nuclear levels but does not lift their degeneracy at all, as it is spherically symmetric (see Figure 8, blue). The electric quadrupole and magnetic dipole interactions cause a splitting of the energy levels of the nucleus (see Figure 8 red and green, respectively).

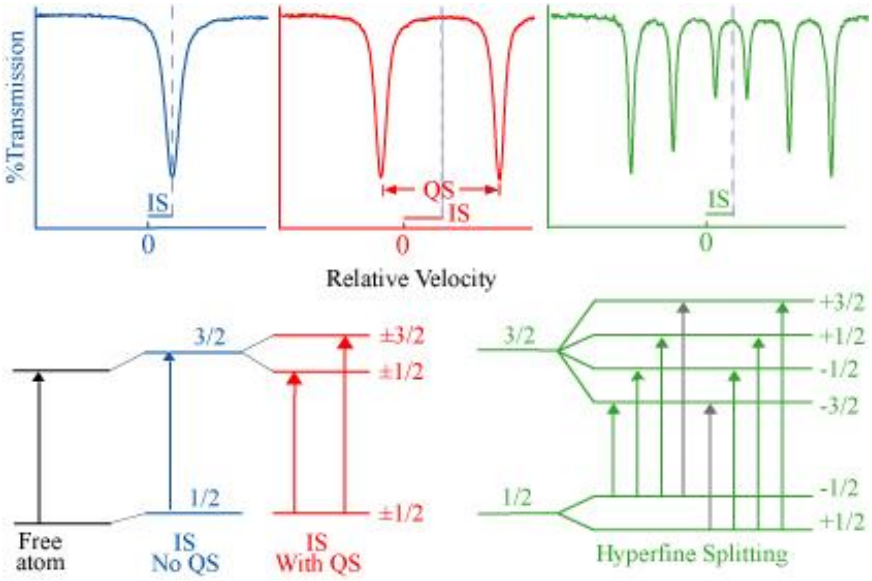

Figure 8: Excitation states of ^{57}Fe.

The plot of absorption vs. velocity (Figure 9) is known as the Mössbauer spectrum. To calibrate the velocity scale, a Mössbauer spectrum of a thin, high-purity, iron metal foil is taken in no magnetic field and at room temperature. The values of the splitting's for the outer, middle and inner pairs of the six-line spectrum are known to be precisely 10.66 mm·s^{-1}, 6.17 mm·s^{-1} and 1.68

$mm \cdot s^{-1}$. The hyperfine field is also known and is approximately 330 kG [21]. Using this information the spectrum can be fitted with a least squares fit [22] in a computer program which centers the spectrum at 0 $mm \cdot s^{-1}$ and finds the velocity increment per channel. Isomer shifts, caused by the electronic monopole interaction can then be quoted relative to this zero velocity channel. Figure 9 is an example of an iron calibration spectrum.

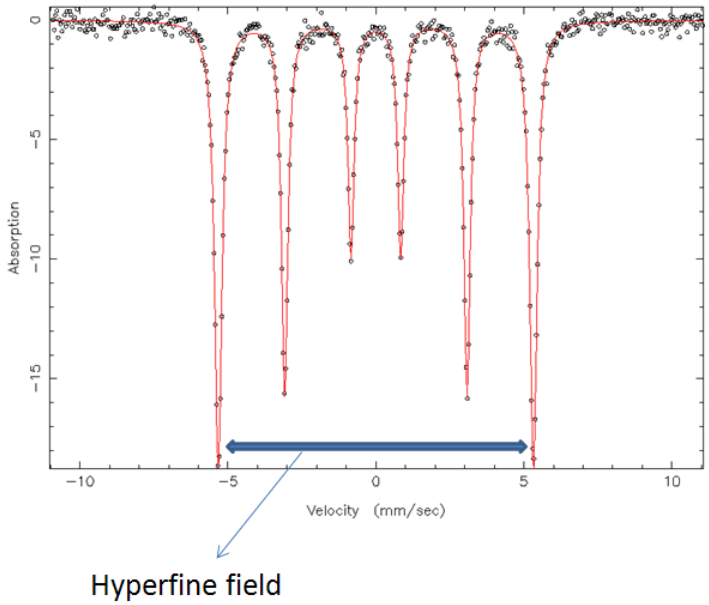

Figure 9: Iron calibration spectrum.

The gamma-ray source

The ^{57}Co source required for the experiments discussed in this thesis was obtained from RITVERC isotope products. The source is produced by placing iron into a cyclotron as a target. The nuclear reaction Fe^{56} (d,n) Co^{57} takes place when a deuterium beam from the reactor strikes a target that absorbs either a proton or a neutron. Trace amounts of ^{57}Co are created in the iron

target. Iron is removed with ether extraction, then ^{57}Co is extracted by electrodeposition onto a rhodium matrix [23], with the rhodium acting as an electrode. The electrode used is usually a material with a cubic lattice crystal structure, which has diamagnetic properties to reduce the splitting of iron levels by internal magnetic and electric effects**.** The rhodium matrix has a thickness of ~6 μm, which allows diffusion of the cobalt ions into the crystal lattice when heated. The radioactive matrix is then placed into a titanium alloy holder with a brazed beryllium window cover. Laser welding seals the edges. The source and its dimensions are shown in Figure 10.

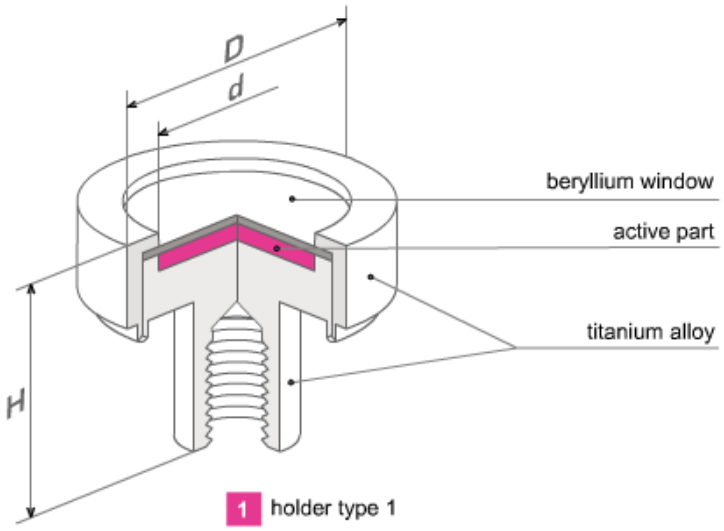

Figure 10: ^{57}Co radioactive source with dimensions D = 11.2mm, H=13 mm and d = 8 mm.

The activity of the source is initially 50 ± 10% mCi, contributing roughly 50,000 counts/second to the spectrum, and has a half-life of 270 days.

The vibrator

To provide a Doppler shift to the gamma rays, the source needs to be mounted onto a vibrator that provides acceleration and deceleration to probe all available energies in an iron spectrum. This vibrator motion, which is controlled by computer program, is run at constant acceleration and synchronized with a multichannel analyzer.

The detector

The detector is a proportional counter filled with krypton gas and a small amount of methane. The methane serves as a quench gas. Krypton is used as it has relatively high sensitivity to gamma rays, since heavier atoms are more "visible" to high-energy photons. In addition, noble gases do not react chemically with any of the components in the detector, leading to a comparatively long lifespan. Details regarding detector function can be found in the Appendix.

The pulse selection can be done with software, which gives a pulse height spectrum. Peaks specifically resulting from the 14.4 keV pulse need to be identified for Mössbauer Spectroscopy. Software also allows the voltage that sets up the electric field needed for the drift to be selected. This electric field needs to be strong enough to prevent recombination of the ion-electron pairs created, but weak enough to differentiate energies. A pulse height spectrum from a proportional krypton counter is shown in Figure 11. The blue and pink shaded regions are useful for Mössbauer experiments.

The short, narrow peak on the far left is due to electronic noise from the equipment, while the blue region is the 2 keV escape peak from the 14.4 keV gamma rays. The short, broad peak next to the 2 keV peak is the 6–7 keV iron x-rays. The main 14.4 keV peak lies in the pink region while the last broad peak is 22–24 keV rhodium x-rays produced by the rhodium matrix of the source. As mentioned previously, the only useful pulses for iron Mössbauer experiments are the

ones generated from the 2 keV escape peak and the 14.4 keV peak in the blue and pink regions, respectively. The other peaks are not useful, as they show up as noise in the Mössbauer spectrum, decreasing signal to noise ratio.

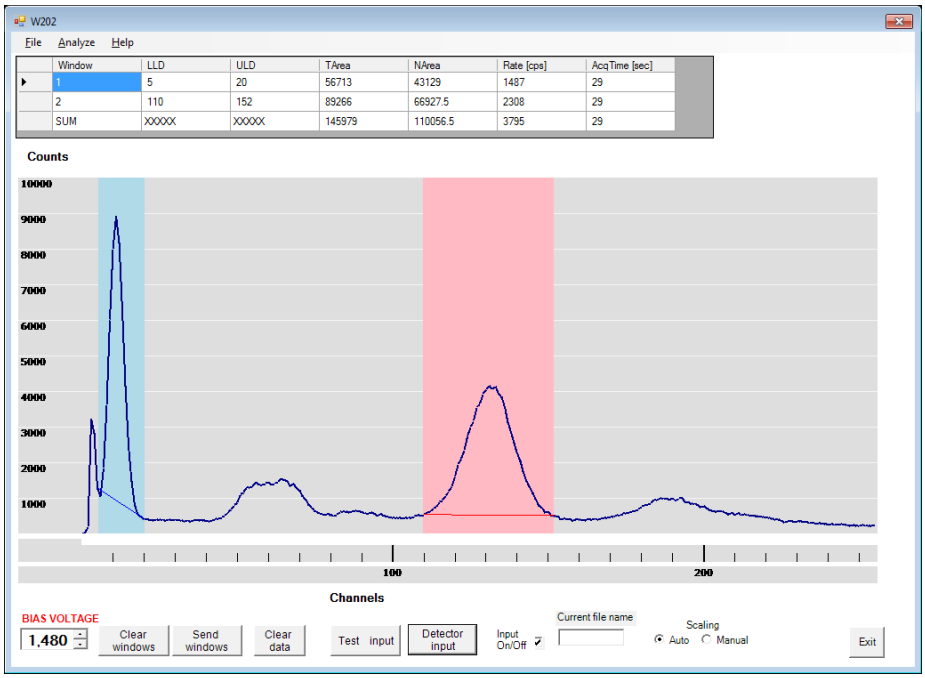

Figure 11: Pulse-height spectrum program.

Room temperature experiments

The apparatus for performing room-temperature experiments is shown in Figure 12. The apparatus is akin to the schematic in Figure 7 and consists of the Mössbauer drive, a source and detector. The sample is placed between the source and the detector and gives a spectrum by absorbing gamma rays. Experiments performed in this manner have an improved counting rate and decreased experiment time compared to those in a cryostat, since the source and the detector can be placed much closer together.

Some experiments were done with a 10 kG neodymium permanent magnet in the room-temperature apparatus (Figure 13) to determine the magnetic properties of the samples. The sample is placed in the center of the magnet in this case.

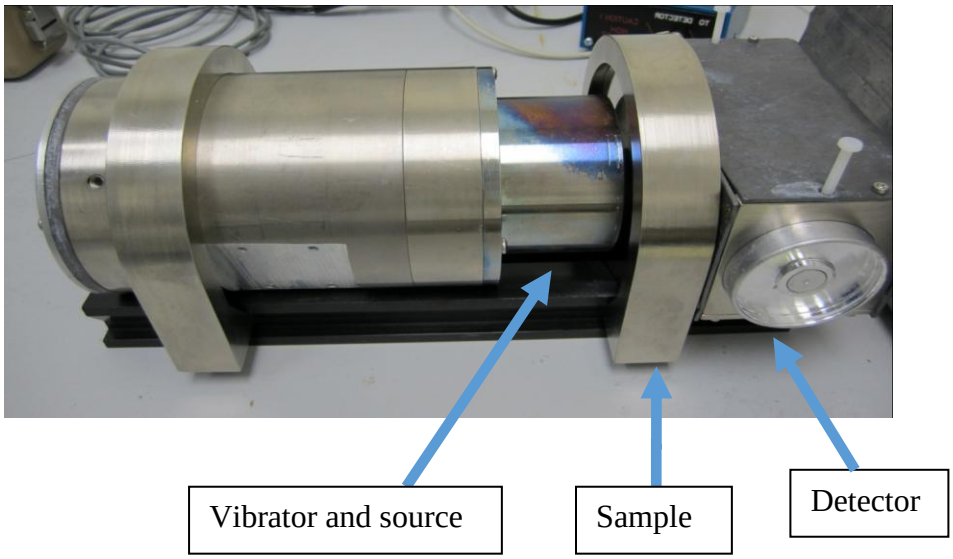

Figure 12: The Mössbauer setup.

Figure 13: Neodymium permanent magnet.

The cryostat

The apparatus used for the low-temperature experiments described here was a closed-cycle refrigerator, in particular, a Janis SHI-850-5. Cryostats of this nature have the advantage of being

able to run for a long time without having to replace helium. The sample is also placed in a cryogen free environment with exposure only to helium gas. These cryostats offer easy sample changing; i.e., the apparatus does not have to return to room temperature, as the cold head and the sample are located in two different compartments. Usually, the cold head would come into contact with the sample. However, in this system the cold head is only in contact with gas around the sample. The refrigerator cools a column of helium gas in the chamber containing the cold head; some time later the sample is inserted into the apparatus with a rod. The sample is then provided with uniform cooling over its entire volume. More detailed workings of the refrigeration cycle for the cryostat will be included in the Appendix.

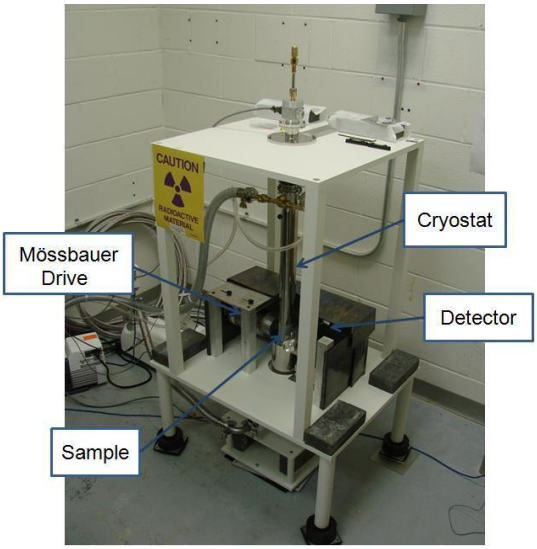

Figure 14: The cryostat with the Mössbauer setup.

The vibrator can be affected by mechanical vibrations that occur during the operation of the cryostat, which complicates the signal gathering and leads to broadened lines in the Mössbauer

spectra. To overcome this problem, the apparatus is placed on top of inflatable rubber mounts. The cryostat setup is shown in Figure 14.

Running samples on the Mössbauer system

The study of iron oxide nanoparticles here was done in different temperature environments; all variable-temperature experiments are done in the cryostat. To prevent oxidation during the transfer of the samples from the glove box to the cryostat, they were placed in a container of liquid nitrogen. The liquid nitrogen prevents the samples from acquiring enough thermal energy to reach the activation energy of various oxidation processes, and the bubbling of nitrogen gas serves to shield the sample from atmospheric oxygen.

The rod that holds the samples is defrosted with warm air prior to transferring the samples to the cryostat. After that, moisture is removed from the surface by drying with a hairdryer. This is to prevent electronic components of the temperature sensors from icing and creating a short circuit. Once the sample is in the cryostat, the chamber is evacuated, then a small amount of helium is introduced for conduction to allow temperature reduction. Once the low temperature (6 K) measurements are completed, the temperature is increased systematically, usually in 20 K increments, up to the Verwey transition temperature region, and in 5 K increments around the Verwey transition temperature (119 K-122 K) itself to capture the possible effects of the transition. These varying temperature experiments are continued until room temperature is reached. Bulk iron oxide was measured as a comparison.

CHAPTER III RESULTS AND DISCUSSION

Objectives

The objectives to keep in mind are as follows:

i. Confirm that the nanoparticles are Fe_3O_4.

ii. Find the blocking temperature and evaluate the magnetic properties of the nanoparticles.

Standard iron calibration

Firstly, a 'standard' iron spectrum has to be taken. At room temperature, ~ 300 K, the iron calibration presents a well-known six-line spectrum. Theoretically, intensity ratios of the lines from outside to inside are expected to be 3:2:1. In reality however, due to thickness effects, these ratios are closer to each other. The intensity of these lines can be modified by magnetization, which is done later in the chapter. This calibration standard is done to make comparisons to experimental spectra. Since the alpha-Fe spectrum is well known, the velocity scale is easily verified.

Table 1: Linewidths for room temperature iron calibration

	Width (mms^{-1})
Width 1	0.30
Width 2	0.26
Width 3	0.24

For the spectrum shown in Figure 9, the velocity parameters were set to achieve a target velocity of 12 mms^{-1}. It was found from the fit that the velocity was ~ 11.42 mms^{-1}. The widths are listed in Table 1.

Width 1 refers to the outside pair of lines located just beyond ±5 mms^{-1}; width 2 refers to the two middle lines and width 3 is the two inner lines. The lines all show relatively narrow widths; the middle two lines, represented by width 3, have theoretical widths of about 0.22 mms^{-1}; a width of 0.249 mms^{-1} is acceptable.

Bulk magnetite

In order to compare fits for the nanoparticles, a fitted spectrum of bulk Fe_3O_4 is used. Figure 15 shows such a spectrum. The bulk sample is initially measured above the Verwey transition temperature with further measurements taken at discreet values below the Verwey transition temperature (119-122 K).

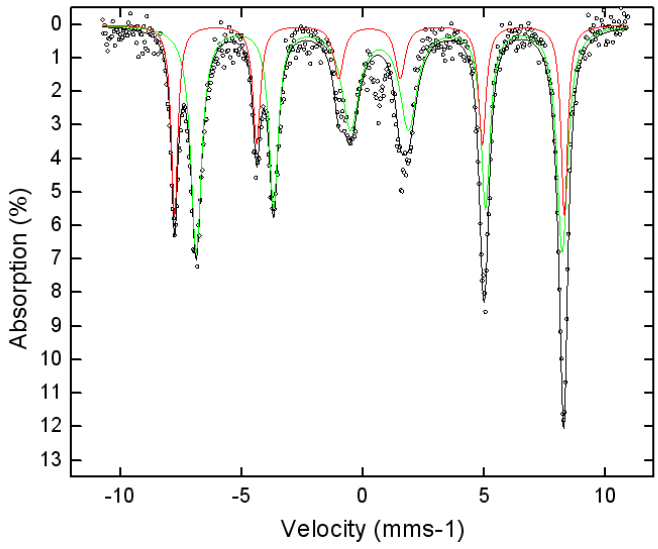

Figure 15: Bulk Fe_3O_4 at room temperature, site A is the red line and site B is green line.

This transition represents the increase of resistivity of Fe_3O_4 when cooled to temperatures below 122 K. A drop in conductivity due to the reordering of the structure of the material will occur

across the transition.Above the Verwey transition temperature at 122K, Fe_3O_4 is known to have an inverse spinel cubic structure and components of $(Fe^{3+})_A$ $(Fe^{3+}Fe^{2+})_B$, with an area ratio of about 1:2 between the A and B sites. This corresponds to the stoichiometry of Fe_3O_4, which is really $FeO{\cdot}Fe_2O_3$. As a result, Fe_3O_4 can also be understood as $(Fe^{3+})_A(2Fe^{2.5+})_B O^{2-}{}_4$ at room temperature. Hence, the octahedral site B is fitted with one green line instead of two separate lines, and site A is fitted with one red line.

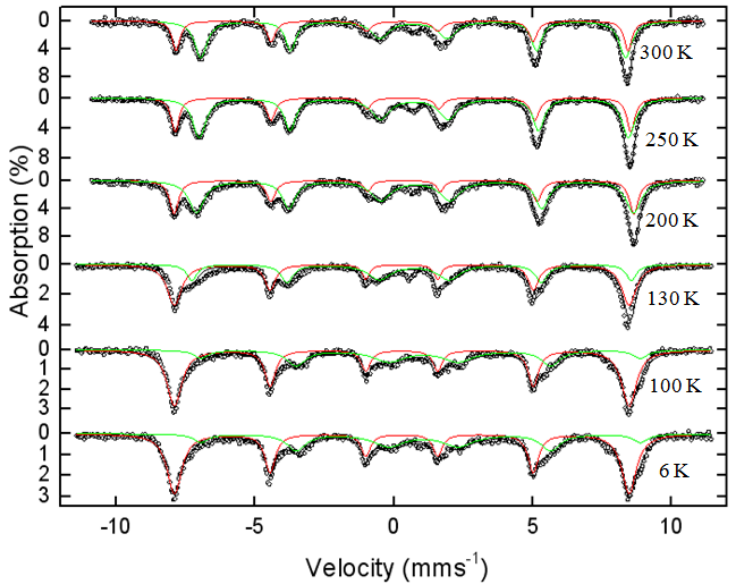

Figure 16: Bulk Fe_3O_4 at varying temperatures, from top, of 300K, 250 K, 200 K, 130 K, 100 K and 6 K

Figure 16 shows a stack plot for bulk Fe_3O_4 at the different temperatures. It is important to examine the behavior of the bulk material under the same conditions as the nanoparticles. The low temperature spectra are found to be similar to those reported by Rubinstein [24], which confirms the material to be bulk Fe_3O_4.

The stacked plot was fitted with the aim of making the A to B site ratios close to 33:67. The red lines indicate the A sites, while B sites are green. The areas under the red and green lines correspond to the 33:67 ratio, with a variance of about 2%.

Table 2: Sample sizes

Sample	Sample Size (nm)
1	5.3
2	10.6
3	11.9

Prior to performing experiments with Mössbauer Spectroscopy, the size of the nanoparticles was measured by our collaborators, using Transmission Electron Microscopy. The nanoparticles have sizes of 5.3 nm (sample 1), 10.6 nm (sample 2) and 11.9 nm (sample 3). The working hypothesis is that the nanoparticles under investigation are small enough to contain single magnetic domains, which fluctuate constantly under ambient conditions [25]. With single domains inside, the particles act like superparamagnets. In superparamagnetic materials, Néel relaxation times are short compared to measurement times ($\tau_m >> \tau$). This causes spectra that are measured at standard temperature and pressure to present broad single lines. The analogous situation for a bulk material would be to increase the temperature of experimentation above the Curie temperature, which is the temperature where ordered magnetic moment oscillations cease to exist for the particular material and disordered oscillations dominate, changing a ferro/ferrimagnetic material into a paramagnet. In this case, a single line is the only spectrum that can be obtained

[26] from Mössbauer Spectroscopy. As a result, the comparisons done to confirm that the nanoparticles are Fe_3O_4 will be at low temperatures where the samples will have their magnetic moments below the blocking temperature and present a distinct six-line spectrum. Spectra of samples obtained at low temperatures will have different shifts compared to those at room temperatures [27].

Confirmation that nanoparticles are magnetite

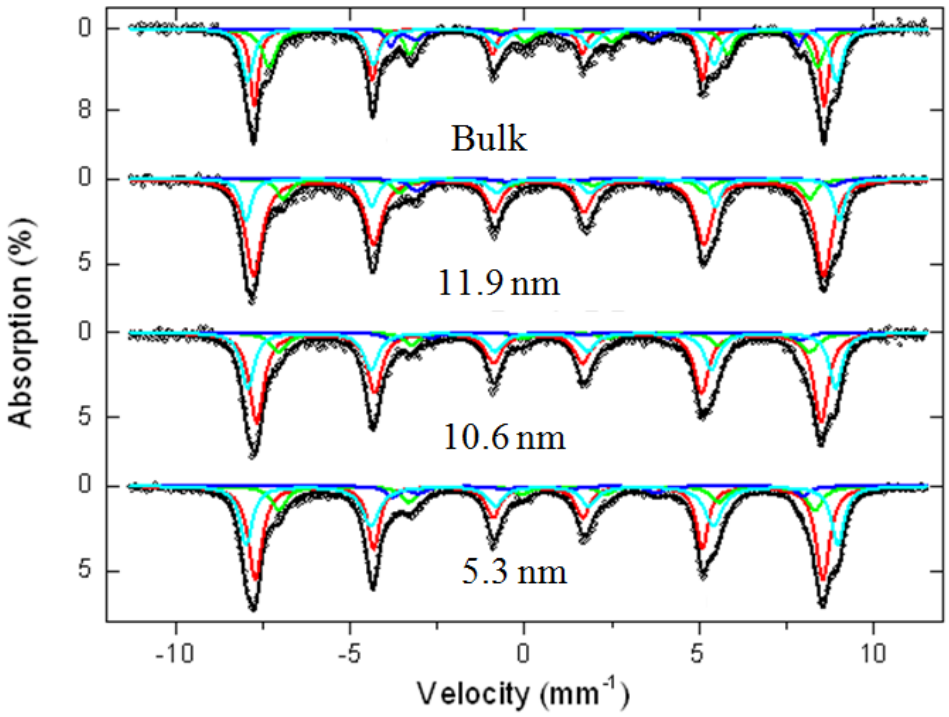

Figure 17: Comparison of Fe_3O_4 bulk and nanoparticles at 6 K.

As mentioned before, these particular sets of experiments will take place at a low temperature. The working hypothesis here is that the nanoparticles will be below their blocking temperature ($\tau_m >> \tau$) at 6 K and will closely resemble bulk Fe_3O_4.

Spectra of the samples in Figure 17 look similar, confirming that the samples of sizes 5.3 nm, 10.6 nm and 11.9 nm are that of Fe_3O_4.

Although there is no consensus as to the actual number of sites at 6 K, the spectra here were fit close to Berry's [28] interpretation. The fits are helpful in determining the widths of the peaks. Also, the fits ensure that features that are prominent and captured in bulk Fe_3O_4 can be found in the nanoparticles. In other words, if the fit with 4 sites can fit both the bulk and the nanoparticles adequately, there is good agreement between the samples. So, it can be concluded here that the nanoparticles are indeed largely Fe_3O_4.

Varying temperature experiments

The hyperfine field strength of a particular sextet can be found from the distance of the first to last line in the spectrum. Figure 16 shows the slight increase of the hyperfine field of the bulk Fe_3O_4 with the decrease in temperature. This is due to an increase of spontaneous magnetization as temperature is decreased. One might expect the same to occur in the nanoparticles.

As shown in Figure 18, there is an increase of the hyperfine field that is proportional to the decrease in temperature in the nanoparticles. Samples 1 (5.3 nm) and 2 (10.6 nm) are single lines at 300 K, with the spectra becoming fully Zeeman split as the temperature is lowered. However, Sample 3 (11.9 nm) is fully Zeeman split at 300 K with the hyperfine field only decreasing with increasing temperature but never fully collapsing into a single line.

The single lines in both Sample 1 and 2 at room temperature show that these samples are superparamagentic and are above their respective blocking temperatures. Sample 3 has a Zemaan split spectrum, but the blocking temperature, if it exists, is higher than the experiment temperatures, as experimental limitations did not allow higher temperatures.

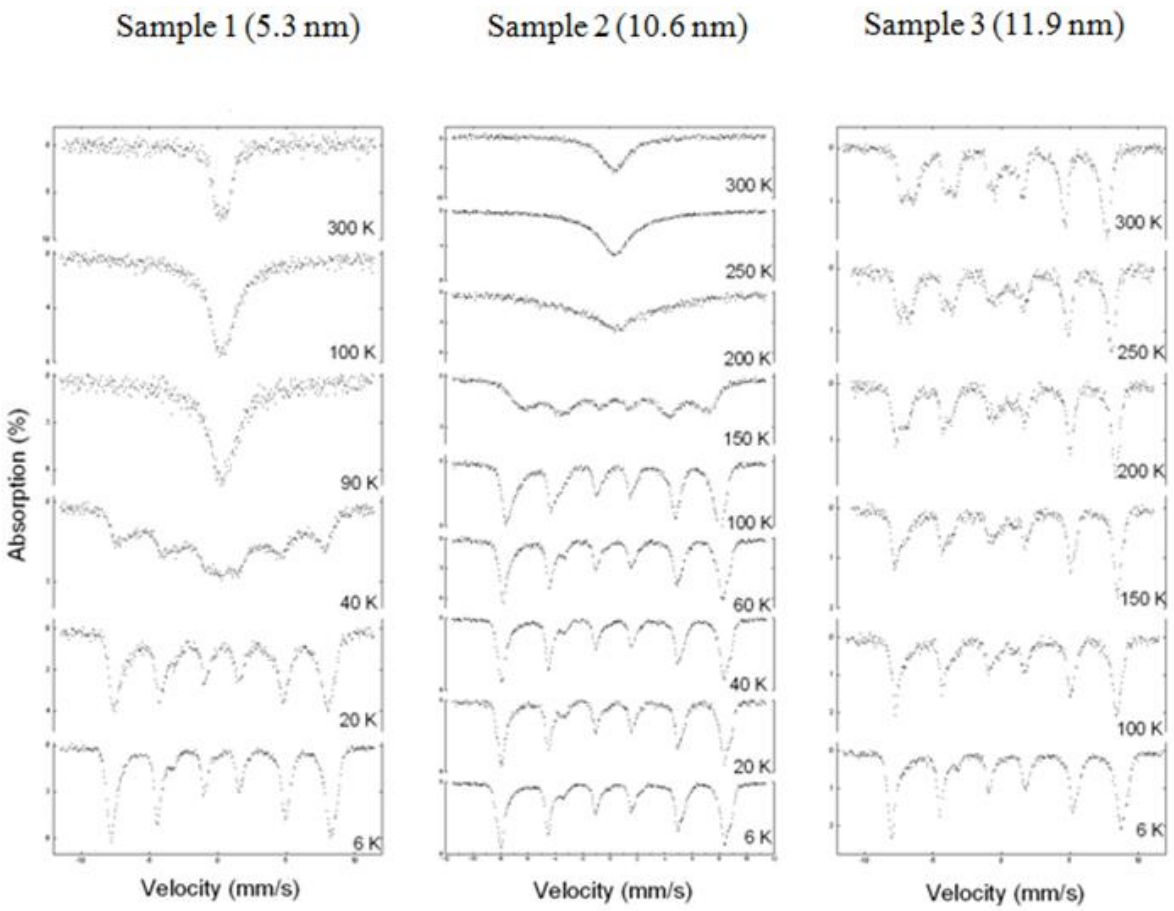

Figure 18: Sample 1, 2 and 3 at varying temperatures

A calculated blocking temperature can be obtained through finding the magnetic anisotropy K. The confirmation of the existence of a blocking temperature can come from the fact that there is a much greater increase in the hyperfine field when temperature is decreased compared to the hyperfine field increase of bulk Fe_3O_4 under the same conditions.

The spectra were fitted with a Lorentzian profile to find the values of the hyperfine fields. The fields were then plotted in Figure 19.

For a magnetic particle, the measured hyperfine field follows the relation:

$B_{hf} = B_{hf}^{(0)} <\cos\theta>$

where θ is the angle between the magnetic moments and the easy axis.

For kT/KV << 1 where the temperature is low, the approximation for <cos θ > can be given as:

$<\cos\theta> = 1 - kT/2KV$

Therefore, the change of the hyperfine field against temperature can be given as:

$$B_{hf} = B_{hf}^{(0)} (1 - kT/2KV) \quad (5)$$

$B_{hf}^{(0)}$ is the hyperfine field at 0 K. T is the experiment temperature and k is Boltzmann's constant. K is the magnetic anisotropy and, V, is the volume of the particles. The volume of the particles is assumed to be a sphere, and the diameters of the spheres are taken from previous TEM measurements.

The data for this region falls within the linear region of magnetization, therefore each sample has been fitted with a least squares function.

As can be seen in Figure 19, the bulk Fe_3O_4 has a hyperfine field that changes very little at these temperatures. Sample 1, 2 and 3 have much larger changes in hyperfine field with the change in

temperature. More importantly, the slope of each of these lines gives the magnetic anisotropy and the energy barrier (Equation 5).

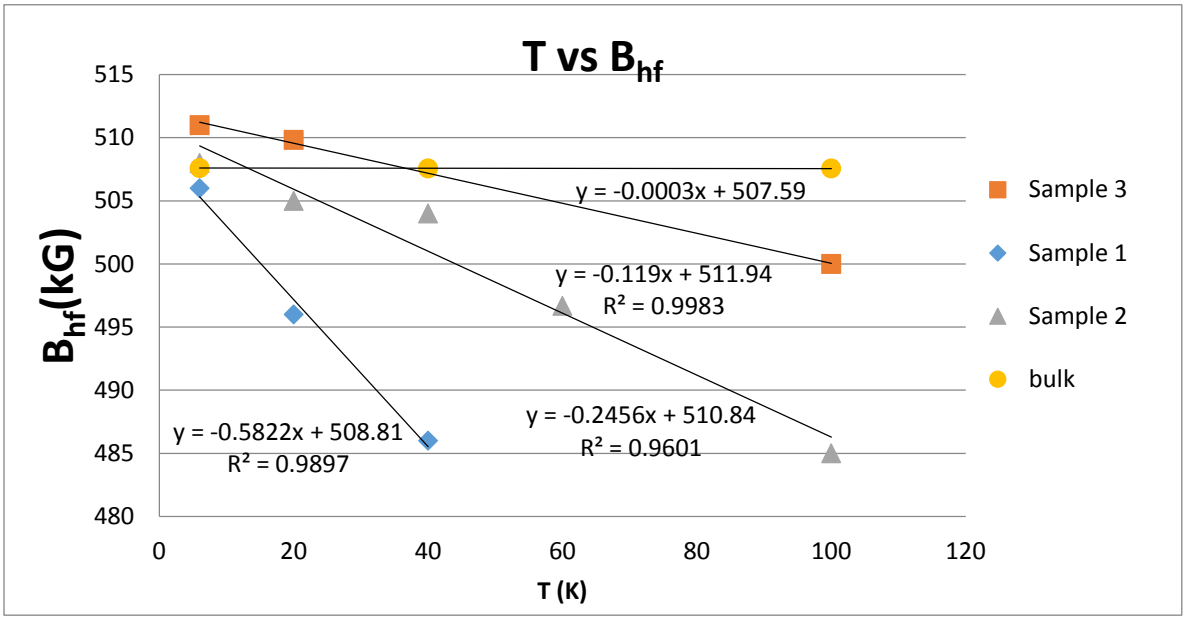

Figure 19: Hyperfine fields of samples 1 (5.3 nm), 2 (10.6 nm) and 3 (11.9 nm) plotted as a function of temperature.

As can be seen in Table 3, to cross the energy barrier and fully magnetize a magnetic particle, a smaller magnetic field would be needed to fully magnetize a smaller particle.

Table 3: Calculated magnetic anisotropy for samples

Sample	Size (nm)	KV (J)	Anisotropy (J/m^3)
1	5.3	0.61E-20	7.77×10^4
2	10.6	1.43E-20	2.30×10^4
3	11.9	2.97E-20	3.37×10^4

The magnetic anisotropy will be important in determining the blocking temperature.

Blocking temperature

Using Equation 3 which was discussed earlier in Chapter I,

$T_B = aKV/k$

where $a = 1/ln(\tau_m/\tau_0)$, and $\tau_0 = 10^{-11}$ s, $\tau_m = 5 \times 10^{-9}$ s [29].

Table 4: Blocking temperature of sample 1, 2 and 3

Sample	T_B (K)
1	70
2	167
3	346

The calculated blocking temperature shows sample 3 has a blocking temperature above room temperature (293 K). This suggests that if a Mössbauer spectrum was taken at 346 K for sample 3, it would have a single line. In Figure 18, a variable temperature set of data for Sample 1, 2 and 3 is done for comparison between the calculated and actual blocking temperatures. From Figure 18 it can be seen that the blocking temperature of sample 1 (5.3 nm) is between 40 K and 90 K, sample 2 (10.6 nm) has a blocking temperature between 150 K and 200 K and sample 3 (11.9 nm) does not have a blocking temperature in the experimental temperature range. For sample 1 and 2, there is good agreement for the calculated and actual blocking temperature. This allows for the conclusion that the calculated blocking temperature for sample 3 is reliable.

Varying magnetic field experiments

As discussed, at room temperature the relaxation of the magnetic moments in the nanoparticles is too short to produce a Zeeman split spectrum for Mössbauer spectroscopy. From previous experiments, it is known that a fully magnetized iron sample in an applied field of parallel direction will have a Mössbauer spectrum with no 2^{nd} and 5^{th} lines. In an applied field of perpendicular direction, the 2^{nd} and 5^{th} lines will have increased intensities. Figure 20 shows the bulk material in varying magnetic fields. It can be seen that the stronger the field, the more distinct the peaks in the spectra become, *i.e.* the peaks overlap less. Furthermore, the areas and intensities of the peaks are modified.

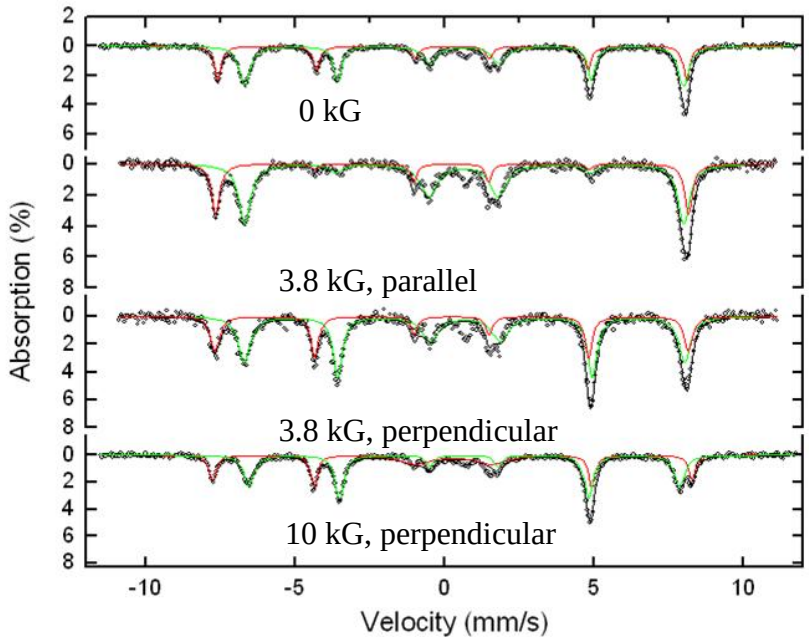

Figure 20: Bulk Fe_3O_4 in magnetic fields, from top to bottom 0 kG, a 3.8 kG parallel field, a 3.8 kG perpendicular field and a 10 kG perpendicular field.

In Figure 20, the Mössbauer spectrum of bulk Fe_3O_4 in a parallel field does have small intensities for the 2nd and 5th lines, which indicates almost complete magnetization. In the absence of a field, bulk Fe_3O_4 maintains the hyperfine fields for site A and B as it is a ferrimagnet and it is below its Curie temperature at room temperature.

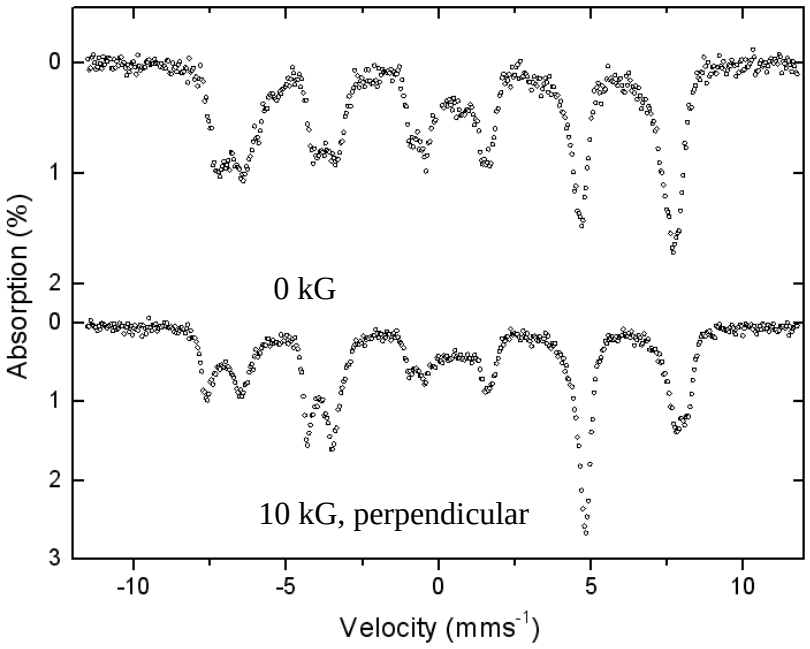

Figure 21: Sample 3 (11.9 nm) at room temperature in magnetic fields, from top, 0 kG and 10 kG in a perpendicular direction

The 10 kG perpendicular magnetic field was applied to Sample 3 (11.9 nm) (Figure 21). Compared to that in 0 kG, the spectrum of Sample 3 in 10 kG has increased intensity in the 2nd and 5th lines.

Sample 3 (11.9 nm) at room temperature has a Mössbauer spectrum similar to that of bulk Fe_3O_4. This corresponds to the earlier discussion that the blocking temperature of sample 3 is higher than room temperature, hence the Zeeman split spectrum.

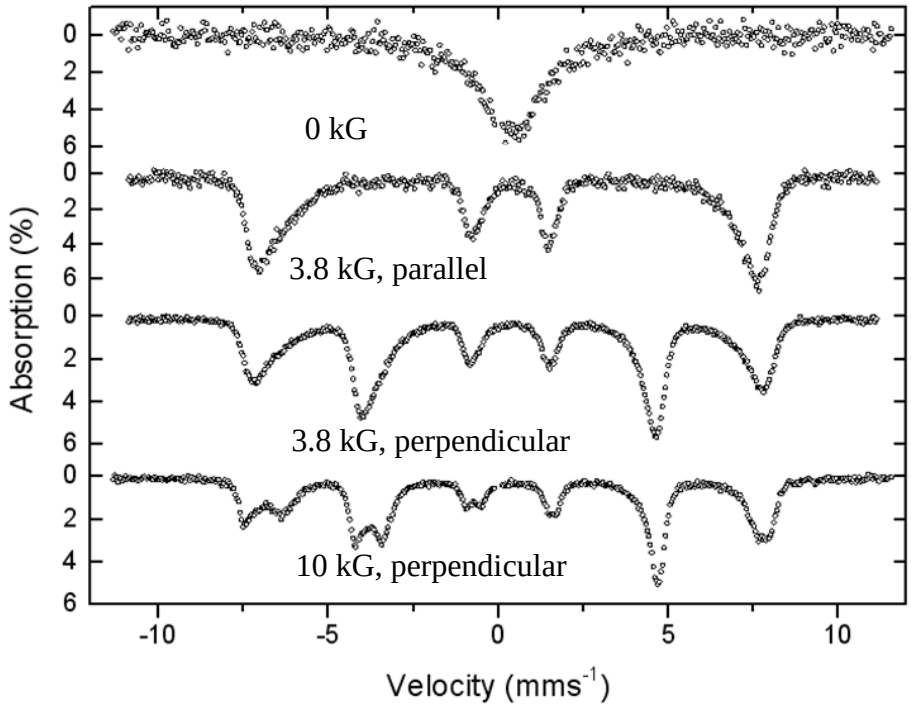

Figure 22: Sample 2 (10.6 nm) in magnetic fields of 0 kG, a 3.8 kG parallel field, a 3.8 kG perpendicular field and a 10 kG perpendicular field.

Sample 2 (10.6 nm) in varying magnetic fields is shown in Figure 22. Similar to Sample 1, this features a single line in the absence of a magnetic field. As mentioned previously, Sample 2 is superparamagnetic at room temperature. In a magnetic field parallel to the 3.8 kG magnetic field, there is a complete absence of the 2nd and 5th lines. In the 3.8 kG perpendicular magnetic field, it can be seen that the 2nd and 5th lines have increased in intensity. Applying a 10 kG field in the

perpendicular direction allows for site A and B to be separated. This leads to the slight decrease in intensity for the 2nd and 5th lines, since site A and B are no longer stacked together.

Sample 2 (10.6 nm) (Figure 22) can be more easily magnetized than Sample 1 (5.3 nm) (Figure 23) as indicated by sharper peaks in the spectra when the same magnetic fields are applied. Furthermore, the 3.8 kG parallel field is able to magnetize sample 2 to the extent that the 2nd and 5th lines are absent, whereas in the same field for Sample 1, no outside peaks can be found definitively (1st, 2nd,5th, 6th lines). This points to Sample 2 having a larger magnetic moment than Sample 1.

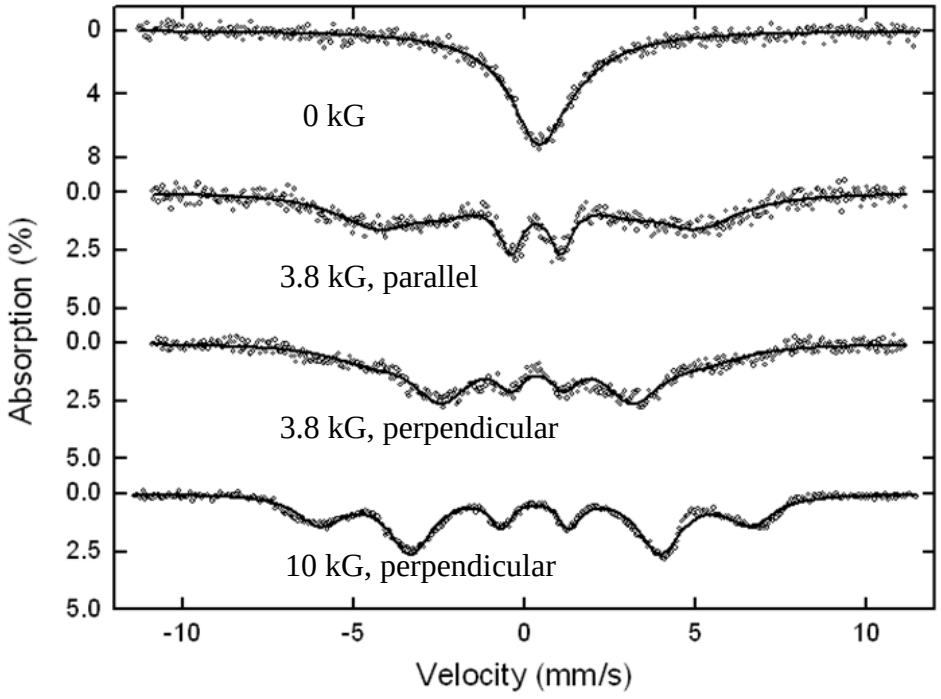

Figure 23: Sample 1 (5.3 nm) in magnetic fields, from top to bottom of 0 kG, a 3.8 kG parallel field, a 3.8 kG perpendicular field and a 10 kG perpendicular field.

For Figure 23, in the absence of a field, the Mössbauer spectrum presents a single line. With increasing magnetic field, the spectrum splits.

The single line in 0 kG means that the sample is superparamagnetic at room temperature. However, due to the fast relaxation times compared to Mössbauer measurement times, a 3.8 kG magnetic field is unable to align the magnetic moments very well and separate out the peaks in the spectrum. In 10 kG, some features can be seen, indicating partial alignment of the magnetic moments to the field. A field bigger than 10 kG is needed to fully magnetize this sample.

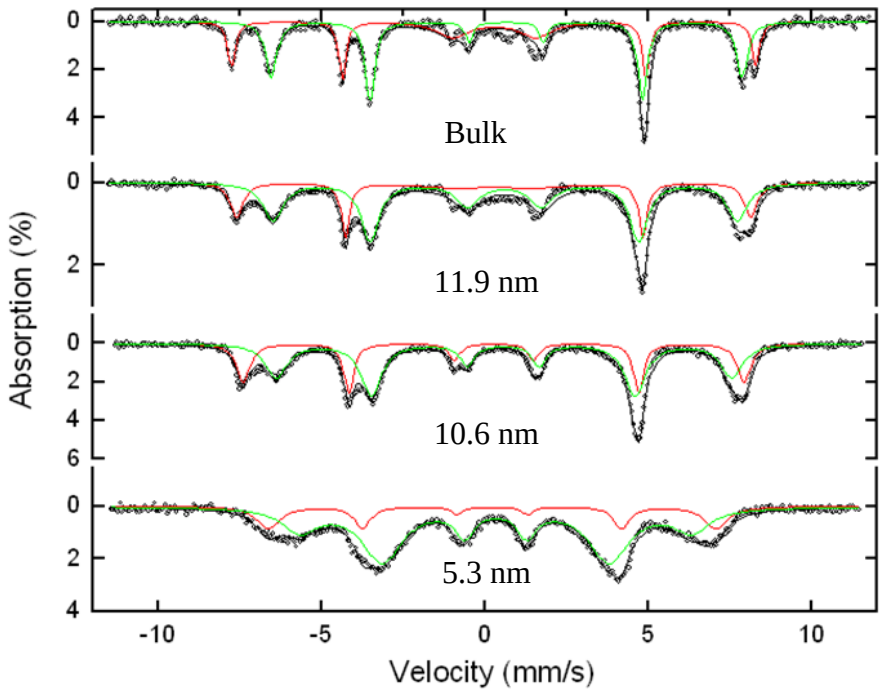

Figure 24: From top to bottom, samples 1 (5.3 nm), 2 (10.6 nm) and 3 (11.9 nm) in a 10 kG perpendicular magnetic field.

To determine which sample has the largest magnetic moment, the Mössbauer spectra in 10 kG can be compared, shown in Figure 24 (plot with 10 kG of bulk and nano). As discussed previously, Sample 2 has a larger magnetic moment than that of Sample 1. It can also be concluded that the magnetic moment of Sample 3 is larger than that of Sample 2 due to more separate and distinct A and B sites.

Therefore, it can be concluded that for single-domain superparamagnetic particles, the bigger the particle the larger the magnetic moment. This is reasonable since a larger domain would be able to contain more magnetic moments.

Langevin Function

Typically, the Langevin function is used for ideal paramagnets. The behavior of superparamagnets is the same as paramagnets in terms of magnetization. The magnetic moments in a superparamagnet will align to an applied magnetic field similar to paramagnets. The difference is that the total magnetic moment in superparamagnets is much greater in magnitude. Using the Langevin function $\mathcal{L}(x)$, and $x=N\mu B/kT$, it can be found that:

$$\frac{\mathbf{B_{hf}}}{\mathbf{B_{hf}(0)}} = \boldsymbol{\mathcal{L}}\left(\frac{\mathbf{gsN\mu B}}{\mathbf{kT}}\right) \quad (6)$$

N is the number of magnetic moments per particle, μ is the Bohr magneton, k the Boltzmann's constant and, T, the temperature of the experiment for the sample. Using an applied field, B, of 10 kG, and gsμ=4/3 Bohr Magnetons, the number of magnetic moments per nanoparticles is shown in Table 5.

Table 5 confirms the finding that was discussed earlier, that the bigger nanoparticle has the bigger total magnetic moment due to a larger amount of small moments per domain.

Table 5: The number of magnetic moments N in a particle

Size (nm)	N *(number of magnetic moments)*
5.3	3.39×10^3
10.6	8.06×10^3
11.9	11.70×10^3

CHAPTER IV CONCLUSION

The objectives of the work were as follows:

i. Confirm that the nanoparticles are Fe_3O_4.

ii. Find the blocking temperature and evaluate the magnetic properties of the nanoparticles.

It was confirmed that the nanoparticles were Fe_3O_4 by comparing Mössbauer spectra of the nanoparticles to that of bulk Fe_3O_4 at 6 K. Figure 17 shows this result.

Above the blocking temperature, superparamagnetic materials present a single line Mössbauer spectrum in the absence of a magnetic field. Here, it is found that both sample 1 (5.3 nm) and sample 2 (10.9 nm) present single-line Mössbauer spectra at room temperature. Sample 3 presents a Zeeman split spectrum at room temperature. This could mean that sample 3 is above its blocking temperature at the experimental temperatures. Since experimental limitations did not allow for experiments higher than room temperature, the blocking temperature of Sample 3 was estimated using Equation 3, which defines the blocking temperature to be when $\tau_m = \tau_N$. By calculating the magnetic anisotropy using Equation 5, the blocking temperature of Sample 3 is found to be 346 K. Similarly, Sample 1 was found to have a blocking temperature of 70 K and sample 2, 167 K, which agrees with experimental results in Figure 18. Applying a magnetic field to the nanoparticles can give an indication of the magnitude of magnetic moments. Here it is found that Sample 1 is only partially magnetized in a 10 kG perpendicular field and only a sextet can be found. For Sample 2 in a 10 kG perpendicular field, two sets of sextets representing the A and B sites can be found, indicating increased magnetization. Sample 3 has the largest magnetization as the spectrum in 10 kG shows sharper peaks for both sextets. It can be concluded that the total magnetic moment is largest for Sample 3, which is reasonable due to it

having the largest volume. In a single-domain nanoparticle, a larger volume contains larger numbers of magnetic moments within.

To confirm this, the Langevin function (Equation 6) was used. The N that was computed from the function represents the total number of magnetic moments. It is found that the largest N is in Sample 1, giving it the largest total magnetic moment.

LIST OF REFERENCES

[1] P. Kucheryavy, J. He, V.T. John, P. Maharjan, L. Spinu, G.Z. Goloverda, V.L. Kolesnichenko, Superparamagnetic iron oxide nanoparticles with variable size and an iron oxidation state as prospective imaging agents, Langmuir : the ACS journal of surfaces and colloids, 29 (2013) 710-716.
[2] R. Hergt, S. Dutz, R. Müller, M. Zeisberger, Magnetic particle hyperthermia: nanoparticle magnetism and materials development for cancer therapy, Journal of Physics: Condensed Matter, 18 (2006) S2919-S2934.
[3] B.J. Evans, 57Fe Hyperfine Fields in Magnetite (Fe3O4), Journal of Applied Physics, 40 (1969) 1411.
[4] J.M. Zuo, J.C.H. Spence, Charge ordering in magnetite at low temperatures, Physical Review B, 42 (1990) 8451-8464.
[5] I. Dézsi, C. Fetzer, Phase transition in nanomagnetite, Journal of Applied Physics, 103 (2008) 104312.
[6] A.P.C. Teixeira, J.C. Tristão, M.H. Araujo, L.C.A. Oliveira, F.C.C. Moura, J.D. Ardisson, C.C. Amorimd, R.M. Lago, Iron a Versatile Element to Produce Materials for Environmental Applications, J. Braz. Chem. Soc., 23 (2012) 1579-1593.
[7] J. García, G. Subías, The Verwey transition—a new perspective, Journal of Physics: Condensed Matter, 16 (2004) R145-R178.
[8] G.A. Sawatzky, Mössbauer Study of Electron Hopping in the Octahedral Sites of Fe3O4, Journal of Applied Physics, 40 (1969) 1402.
[9] M. Jackson, B. Moskowitz, J. Bowles, Interpretation of Low-Temperature Data Part III:The Magnetite Verwey Transition, The IRM Quarterly, 20 (2011).
[10] C. Kittel, Introduction to Solid State Physics, 8th Edition (2005).
[11] E. Lima, A.L. Brandl, A.D. Arelaro, G.F. Goya, Spin disorder and magnetic anisotropy in Fe_3O_4 nanoparticles, Journal of Applied Physics, 99 (2006) 083908.
[12] S.K. Banerjee, B.M. Moskowitz, Ferrimagnetic Properties of Magnetite Topics in Geobiology 5(1985) 17-41.
[13] D.J. Dunlop, On the Demagnetizing Energy and Demagnetizing Factor of a Multi-domain Ferromagnetic Cube, Geophysical Research Letters, 10 (1983) 79-82.
[14] D.J. Dunlop, Superparamagnetic and single-domain threshold sizes in magnetite, Journal of Geophysical Research, 78 (1973) 1780-1793.
[15] S. Morup, Mössbauer Studies of Thermal Excitations in Magnetically Ordered Microcrystals, Appl. Phys, (1976) 63-66.
[16] S.H. Kilcoyne, Ferritin: a model superparamagnet, Journal of Magnetism and Magnetic Materials 140-144 (1995) 1466-1467.
[17] D.A. Clauter, V.A. Schmidt, Shifts in blocking temperature spectra for magnetite powders as a function of grain size and applied magnetic field, Physics of the Earth and Planetary Interiors, 26 (1981) 81-92.
[18] G.K. Wertheim, Mössbauer effect: principles and applications, Academic Press, 1964.
[19] R. Housley, F. Hess, Analysis of Debye-Waller-Factor and Mössbauer-Thermal-Shift Measurements. I. General Theory, Physical Review, 146 (1966) 517-526.
[20] G. Goloverda, B. Jackson, C. Kidd, V. Kolesnichenko, Synthesis of ultrasmall magnetic iron oxide nanoparticles and study of their colloid and surface chemistry, J Magn Magn Mater, 321 (2009) 1372-1376.

[21] R.S. Preston, S.S. Hanna, J. Heberle, Mössbauer Effect in Metallic Iron, Physical Review, 128 (1962) 2207-2218.
[22] R.S.H.a.W. Kundig, Mössbauer measurements of magnetite below the Verwey transition, Solid State Communications,, 8 (1970) 303-308,.
[23] I. Cieszykowska, M. Zoltowska, M. Mielcarski, Electrodeposition of carrier-free 57Co on rhodium as an approach to the preparation of Mössbauer sources, Applied radiation and isotopes : including data, instrumentation and methods for use in agriculture, industry and medicine, 69 (2011) 142-145.
[24] M.R.a.D.W. Forester, Investigation of the insulating phase of magnetite by NMR and the Mössbauer effect, Solid State Communications, 9 (1971) 1675—1679.
[25] J.M. Greneche, Structural andMagnetic Properties of Nanostructured Oxides Investigated by ^{57}Fe Mössbauer Spectrometry, Hyperfine Interactions, 148/149 (2003) 79–89.
[26] L. Haggstrom, H. Annersten, T. Ericsson, R. Wappling, W. Karner, S. Bjarman, Magnetic Dipolar and Electric Quadrupolar Effects on Mössbauer Spectra of Magnetite Above the Verwey Transition, Hyperfine Interactions, 5 (1978) 201-214.
[27] S.N.a.Y. Murakami, Second-Order Doppler Shift of Fe^{57} Mössbauer Resonance in A1-0.01% Fe^{57} Alloy Solid Solution, Phys. Stat. Sol., (b) (1971) 711
[28] F.J. Berry, Mössbauer spectroscopic examination of a single crystal of Fe3O4, J. Phys.: Condens. Matter, (1998) 215–220.
[29] S.G. H-Y. Hah, C. E. Johnson, J. A. Johnson, V. Kolesnichenko, P. Kucheryavy, G. Goloverda, Line Narrowing in Mössbauer Spectra of Superparamagnetic Fe_3O_4 Nanoparticles, Journal of Physics: Conference Series, 548 (2014).
[30] W.E. Gifford, The Gifford-McMahon Cycle, Advances in Cryogenic Engineering 11 (1966) 152-159

APPENDIX

The vibrator

For experiments relating to iron, the velocity ranges are usually between -12 $mm \cdot s^{-1}$ and +12 $mm \cdot s^{-1}$, as this range covers all the spectral lines for iron-based samples.

To set the velocity, the signal produced by the master vibrator should be scaled to the vibrator. The computer program has default settings for the most popular velocity range $\pm 12 mm \cdot s^{-1}$. However, at certain times, some lines approach the edges of the range and a wider range is needed. The software allows the user to manually input the voltages to change the velocities. Since it is known that the vibrator velocity is directly proportional to the signal produced by the master vibrator, all that needs to be done is to scale the potentials appropriately.

The detector

A positively charged wire serves as an electrode in the counter. When the photons emitted from the source enter the counter through the window and ionize the krypton gas in the chamber, the electrons drift to the wire while the positive ions drift to the boundaries of the detector. The highly mobile electrons have enough energy to continue ionizing the krypton on their trajectory towards the electrode; this creates ion-electron pairs, which in turn can potentially ionize more atoms when drifting, amplifying the signal. The ionization of multiple atoms by the electron drift takes place in a small area away from the electrode, where the field is stronger. This is the avalanche region and is illustrated in Figure 25.

The methane gas suppresses random drifts of electrons, thus minimizing the distance for the electrons to reach the electrode. In addition to the main 14.4 keV pulse, photons of energies 122 keV and 136 keV generated by the source also enter the gas chamber, but their high energy causes them to be less visible to the Krypton and they can only produce scattering at lower energies. Such scattering creates a background that shows up as noise in the spectra; although the

single-channel analyzer can filter some of this, ~20 % of the 14.4 keV pulse present in the pulse height spectrum is from this scattering.

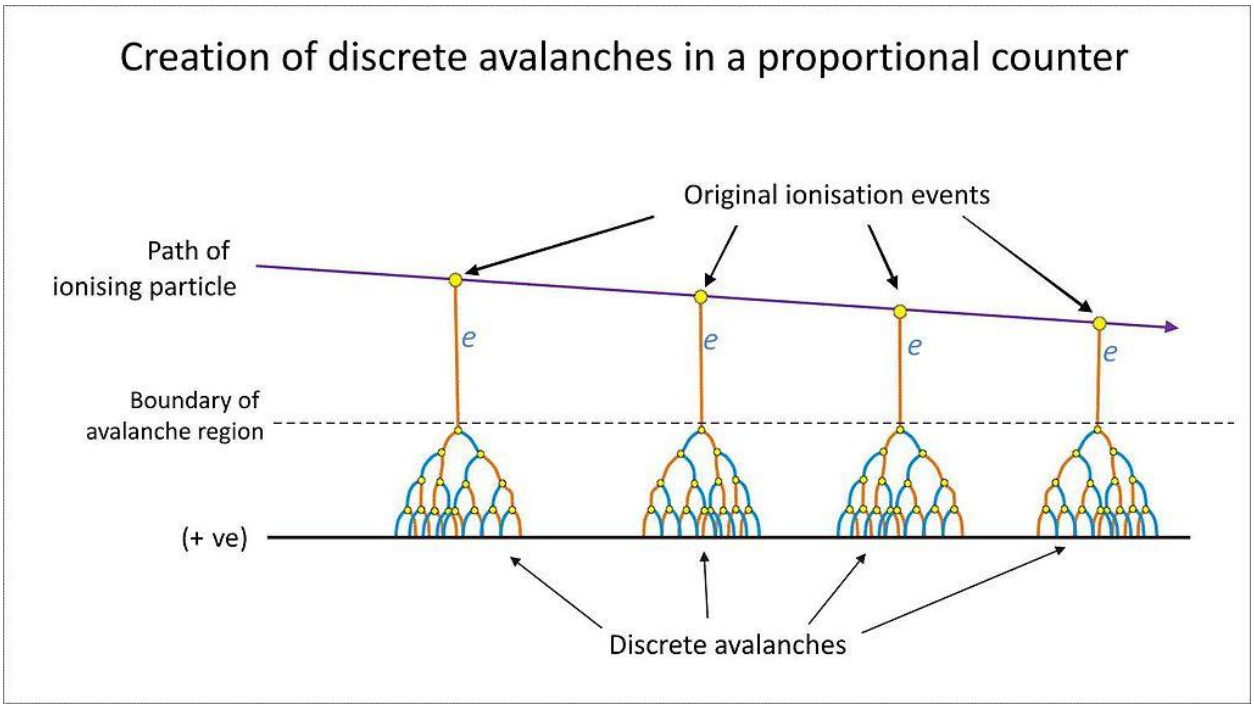

Figure 25: Creation of discrete avalanches, wire contains positive charge.

The signal from the counter is electronically amplified before being sent to the single-channel analyzer to selectively view the 14.4 keV pulse.

The cryostat

The cryostat works according to the Gifford-McMahon Refrigeration cycle [30], cooling the cold head, which cools the helium gas around the sample and in turn cools the sample. The compressor contains two valves. First, the compressed helium gas is pumped into the displacer chamber through the high-pressure valve. The gas is subsequently pumped back into the

compressor through the low-pressure valve. The displacer is held in place with the high-pressure valve closed, and the volume expansion causes the gas to cool rapidly. The displacer is allowed to completely compress the remaining volume after that, which pumps the cooled gas back to the compressor through the low-pressure valve, carrying heat away from the cold head. This cycle is repeated indefinitely until the compressor is shut down. This cycle is described as being a closed cycle as the helium gas in the compressor is never exposed to the atmosphere. Figure 26 illustrates the Gifford-McMahon cycle.

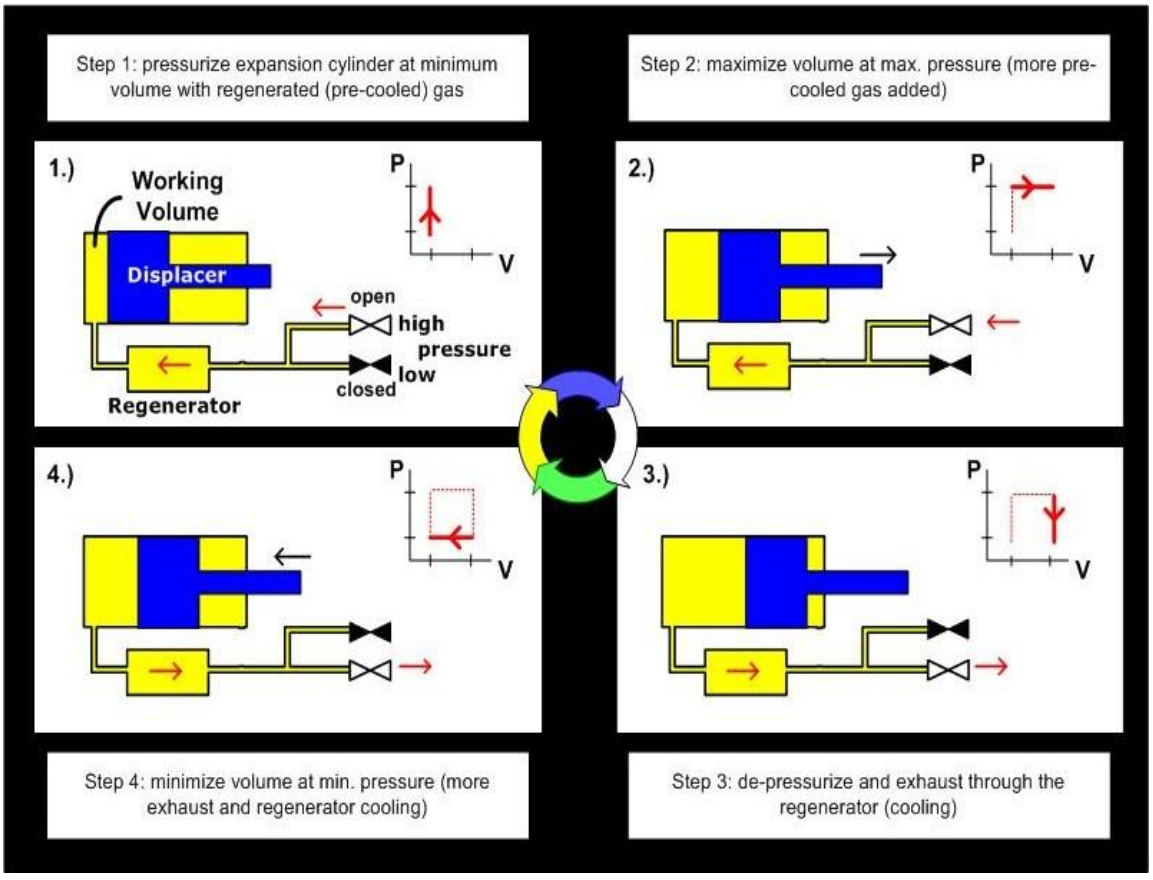

Figure 26: The Gifford-McMahon cycle.

The heat collected by the compressor needs to be removed from the system; this is done by allowing water to flow through the system into a sink. Alternatively an ethylene glycol coolant can be used. The pressure of the gas within the compressor is crucial; it has an operating pressure of ~2.1 MPa and a static pressure of ~ 1.6 MPa. However, the system does have the drawback of vibrations.

VITA

Hien-Yoong Hah grew up in Malaysia with parents who worked hard to make sure he stayed in school. He is the eldest of three children, and counts himself one of the luckiest people on Earth. With great luck he attended and graduated from Coe College with a bachelor's degree in Physics. By chance, he met Dr Jackie Johnson who accepted him as a graduate student in the Biomedical Engineering department at University of Tennessee Space Institute. Also seemingly by coincidence, Dr Charles Johnson, one of the most learned researchers in Mössbauer Spectroscopy was available to help and mentor Hien-Yoong with his masters work in magnetite using Mössbauer Spectroscopy. Hien-Yoong completed his master's work in August 2015, with the intent to furthering his education.